



Intraseasonal Air–Sea Interaction Over the Southeastern Indian Ocean and its Impact on Indian Summer Monsoon

Ze Meng¹, Lei Zhou^{1,2*}, Jianhuang Qin³ and Baosheng Li⁴

¹School of Oceanography, Shanghai Jiao Tong University, Shanghai, China, ²Southern Marine Science and Engineering Guangdong Laboratory (Zhuhai), Zhuhai, China, ³College of Oceanography, Hohai University, Nanjing, China, ⁴State Key Laboratory of Satellite Ocean Environment Dynamics, Second Institute of Oceanography, Ministry of Natural Resources, Hangzhou, China

OPEN ACCESS

Edited by:

Jinbao Song,
Zhejiang University, China

Reviewed by:

Jiangyu Mao,
Institute of Atmospheric Physics
(CAS), China
Youmin Tang,
University of Northern British
Columbia Canada, Canada

*Correspondence:

Lei Zhou
zhoulei1588@sjtu.edu.cn

Specialty section:

This article was submitted to
Physical Oceanography,
a section of the journal
Frontiers in Marine Science

Received: 16 April 2022

Accepted: 30 May 2022

Published: 12 July 2022

Citation:

Meng Z, Zhou L, Qin J and Li B
(2022) Intraseasonal Air–Sea
Interaction Over the Southeastern
Indian Ocean and its Impact on
Indian Summer Monsoon.
Front. Mar. Sci. 9:921585.
doi: 10.3389/fmars.2022.921585

The weak monsoon rainfall simulation in the CMIP6 models calls for further process understanding about the Indian summer monsoon (ISM), especially the intraseasonal variabilities. Here, the remote forcing from the Southern Hemisphere on the Indian summer monsoon is examined. Over the southeastern Indian Ocean (SEIO), intraseasonal warm SST anomalies can induce low-level southeasterly wind anomalies and accelerate the background southeasterly wind. According to the mechanism of Wind-Evaporation-SST (WES) feedback, the wind acceleration gives rise to the positive anomalies of surface latent heat flux (LHF). The intraseasonal wind anomalies propagate equatorward along with the background southeasterlies; the positive LHF increases the moist static energy over the equator. As a result, deep convections are reinforced over tropics, which strengthen the northward-propagating monsoon intraseasonal oscillations. During boreal summer, the northward intraseasonal oscillation prompts enhanced rainfall events over the monsoon region. Current results indicate the inter-hemispheric impacts as an inevitable contributor to the heavy precipitation during ISM in the Northern Hemisphere. In CMIP6, the models with better SST simulations over SEIO can have stronger equatorial rainfall and more realistic northward propagation. The unsatisfactory simulations of CMIP6 are associated with the defective ocean–atmosphere interaction over SEIO, and one clue is the feeble variances of intraseasonal oceanic signals over SEIO, which is far from the observation. This research offers a new perspective on the chronic dry monsoon bias in the Northern Hemisphere; the cross-equatorial process and the bias of intraseasonal oceanic variation over SEIO deserve further attention in the coupled models.

Keywords: Southeastern Indian Ocean, ocean–atmosphere interaction, intraseasonal variability (ISV), Indian summer monsoon (ISM), CMIP6

1 INTRODUCTION

Indian summer monsoon (ISM) is an active system in the Northern Hemisphere. The socioeconomic impacts of ISM, such as extreme droughts and floods, can hugely affect the lifeline for nearly one-third of the global population over South Asia (Fu, 2003; Li et al., 2020a; Shi et al., 2021). Although ISM and the associated rainfall events are hot research topics for a long time, the simulation of

monsoonal rainfall still remains a scientific challenge (Wang et al., 2014). Generally, the intraseasonal variability accounts for at least 60% of total rainfall variance, and the associated deficit in simulations is considered as one of the important reasons for the rainfall bias in climate models. For example, in the 3rd and the 5th Coupled Model Inter-comparison Project (CMIP3 and CMIP5; Meehl et al., 2007; Taylor et al., 2012), many evaluations reported the underestimation of monsoon rainfall, especially the insufficient intraseasonal rainfall over the northern Bay of Bengal and the Indian subcontinent (Lin et al., 2008; Hu et al., 2017). Therefore, model simulations of intraseasonal variability appeals for advancing process understanding of the simulated chronic dry bias (Wang et al., 2005).

During ISM, intraseasonal oscillation with a period of 20–100 days [also called Monsoon intraseasonal oscillation (MISO); Goswami et al., 2003], shows a clear northward propagation and brings moisture and momentum from the equator to the monsoon region at higher latitudes. Comprehensive understandings for the northward propagation of MISO are discussed in several previous studies (Jiang et al., 2004; Kang et al., 2010; Li et al., 2021). As a prominent atmospheric oscillation, the dynamics of MISO is one essential concern for ISM variabilities. The development of convection ahead of MISO is associated with barotropic vorticity anomalies driven by the vertical shear of easterly winds (Jiang et al., 2004; Drbohlav and Wang, 2005). Kang et al. (2010) and Liu et al. (2015) concluded that the vertical wind shear also prompted a secondary meridional circulation *via* convective momentum transports and led to convergence in the lower troposphere. The atmospheric meridional advection also plays a role. The moisture in the boundary layer (Jiang et al., 2004; Boos and Kuang, 2010) and the barotropic vorticity (Bellon and Sobel, 2008) are transported northward by either the background or the anomalous winds, which are confirmed by DeMott et al. (2013) in a coupled climate model.

Given that the northward propagation occurs over the tropical Indian Ocean, the air–sea interaction also receives huge attention (Fu et al., 2003; Xi et al., 2015; Gao et al., 2018; Meng et al., 2021). Variations in oceanic signals are discovered along the track of northward-propagating MISO (Hendon and Glick, 1997; Kemball-Cook and Wang, 2001). By causing convergence and destabilizing the boundary layer, SST anomalies (including SST gradients) and the associated surface heat flux can usually reinforce the intensity of convection and modulate the phase speed of the northward propagation (Webster, 1983; Kemball-Cook et al., 2001; Fu et al., 2003). It was demonstrated by Fu et al. (2008) and Hu et al. (2015) that the ocean–atmosphere coupling largely increased the prediction skills of MISO (Li et al., 2020b). Gao et al. (2018) quantified the contributions from SST anomalies to the moist static energy; the value was as high as 20% over the active monsoon regions. In short, although northward propagation is closely linked with the atmospheric dynamics, a better rendition of the oceanic impacts on MISO is favorable for a better simulation of MISO and ISM (Fu and Wang, 2004; Rajendran and Kitoh, 2006; Roxy and Tanimoto, 2007; Weng and Yu, 2010).

Besides the Northern Hemisphere, the remote impacts from the Southern Hemisphere on the ISM have been already examined by some studies (Rodwell, 1997; Gebregiorgis et al., 2018). For

example, the inter-annual Indian Ocean Dipole (IOD, Saji et al., 1999), which includes the abnormal SST anomalies over southeastern Indian Ocean (SEIO) and western Indian Ocean, is one of the most pronounced climate modes over the Indian Ocean and is reported to play a role (Saji and Yamagata, 2003; Ashok et al., 2004). Ratna et al. (2021) unveiled that the positive IOD in 2019 promoted an unusual seasonal evolution of ISM. Ashok et al. (2001) and Guan et al. (2003) demonstrated the association between IOD and the convergence/divergence over the Bay of Bengal, which further affects the interannual ISM. Ajayamohan and Rao (2008) connect the frequent IOD with the increasing extreme rainfall during ISM under the ongoing warming trend of Indian Ocean in the last few decades. Nevertheless, these studies mainly focused on the seasonal and even longer timescales. The possible cross-hemisphere teleconnection at intraseasonal timescales is still missing.

In this study, we show the mechanisms of the intraseasonal ocean–atmosphere interaction over the southeastern Indian Ocean (SEIO), its association with the monsoon rainfall in the Northern Hemisphere, and the bias of model simulations. The rest of this paper is organized as follows. Data and methods are introduced in Section 2. The biases of intraseasonal variabilities in the latest 6th Coupled Model Inter-comparison Project (CMIP6, Eyring et al., 2016), the associated mechanism of ocean–atmosphere interaction over SEIO, and its contribution to monsoon rainfall are presented in Section 3. Conclusions and discussion are presented in Section 4.

2 DATA AND METHODS

2.1 Data

SST and sea surface heat fluxes (including latent and sensible heat fluxes and net shortwave and longwave radiation) are obtained from objectively analyzed ocean–atmosphere fluxes (OAFlux), version 3 (Yu and Weller, 2007). The horizontal resolution is 0.25° latitude \times 0.25° longitude. Precipitation is obtained from Tropical Rainfall Measuring Mission (TRMM, Huffman et al., 2007) and the horizontal resolution is 1° latitude \times 1° longitude. Atmospheric variables such as specific humidity, air temperature, geopotential height, atmospheric winds, and outgoing longwave radiation (OLR) are obtained from ECMWF Reanalysis 5th Generation (ERA5; Hersbach et al., 2020). The horizontal resolution is 1° latitude \times 1° longitude. Besides, 20 CMIP6 models that provide daily surface heat fluxes, OLR, precipitation, and SST are used. For each CMIP6 model, the first realization (r1i1p1f1) of the historical simulations is chosen. Specific information of each CMIP6 model is listed in **Table 1** (also see <https://esgf-node.llnl.gov/projects/cmip6/>). Considering the different horizontal resolutions between model outputs and (re-) analysis datasets, all of them are interpolated into a common rectangular grid of 2.5° latitude \times 2.5° longitude. In order to resolve the intraseasonal variabilities, all above analysis dataset, re-analysis datasets, and model outputs are daily scale. The ISVs are defined as the signals with their period of 20–100 days, and the main focus is boreal summer (from June to September). To be compatible with CMIP6, all the datasets are obtained from 1985 to 2014.

TABLE 1 | List of CMIP6 models included in this study.

CMIP6 models	Institute/Country	Atmospheric Grids	SST Grids	Cases of SEIO SST events
ACCESS-CM2	CSIRO/BOM, Australia	192×144	360×300	55
ACCESS-ESM1-5		192×144	360×300	61
BCC-CSM2-MR	BCC, CMA, China	320×160	360×232	52
BCC-ESM1		128×64	360×232	58
CanESM5	CCCMA, Canada	128×64	360×291	44
CESM2	NCAR, USA	288×192	320×384	58
CESM2-FV2		144×96	320×384	57
CESM2-WACCM-FV2		144×96	320×384	61
EC-Earth3-Veg	EC-Earth-Consortium, European Community	512×256	362×292	49
GFDL-CM4	NOAA GFDL, USA	144×90	1440×1080	62
IPSL-CM6A-LR	IPSL, France	144×143	362×332	56
MIROC6	MIROC, Japan	256×128	360×256	51
MPI-ESM-1-2-HAM	MPI-M, Germany	192×96	256×220	54
MPI-ESM1-2-HR		384×192	802×404	48
MPI-ESM1-2-LR		192×96	256×220	57
MRI-ESM2-0	MRI, Japan	320×160	360×363	49
NESM3	NUIST, China	192×96	362×292	49
NorESM2-LM	NCC, Norway	144×96	360×385	53
NorESM2-MM		288×192	360×385	53
SAM0-UNICON	SNU, Korea	288×192	320×384	46

All the included models provide variables for our analysis: daily SST, LHF, SHF, surface wind speed, surface air humidity, and atmospheric moisture. For fair comparisons, the first realization (r1i1p1f1) of the historical simulations is chosen model in each CMIP6 model. The time period is from 1985 to 2014.

2.2 Method

Warm SST anomalies are favorable for energetic ocean-atmosphere interactions. However, warm SST anomalies alone do not guarantee such an impact, since the surface heat flux needs to be enhanced so that the atmosphere can feel the oceanic variation (Sobel et al., 2008). The LHF is estimated as (Cayan, 1992; DeMott et al., 2016)

$$LHF = \rho_0 C_d L_v V (q_{sst} - q_a) \dots (1),$$

where $\rho_0 = 1.3\text{kg/m}^3$ is the air density; $C_d = 1.35 \times 10^{-3}$ is the exchange coefficient for latent heat; $L_v = 2.5 \times 10^6 \text{J/kg}$ is the latent heat of vaporization; V is the wind speed near the surface; q_{sst} is the saturated specific humidity at the temperature of SST; and q_a is the near-surface specific humidity. q_{sst} is estimated with $\frac{\epsilon}{p} A e^{\frac{B}{T}}$

(Hendon and Glick, 1997), where p is the surface pressure, T represents SST, $\epsilon = 0.622$, $A = 2.53 \times 10^8 \text{kPa}$, and $B = 2.5 \times 10^6 \text{K}$. Most variables can be decomposed into two scales. One is the low-frequency or the background component, which has a period longer than 100 days. The other one is the perturbation or the intraseasonal component with a period between 20 and 100 days. The high-frequency components with a period shorter than 20 days can also be included in the decomposition (Zhou and Murtugudde, 2014). However, none of the components containing the high-frequency variabilities are found to be large enough, so that they can be ignored. The background component is denoted with an overbar, and the intraseasonal component is denoted with a prime. For example, $T = \bar{T} + T'$. Therefore, the intraseasonal LHF can be written as

$$\begin{aligned}
 LHF' = & \rho_0 C_d L_v [\bar{V} \left(\frac{\epsilon}{p} A e^{\frac{B}{\bar{T}}} \cdot \frac{BT'}{\bar{T}^2} - \bar{q}'_a \right)] \text{(I)} \\
 & + V' \left(\frac{\epsilon}{p} A e^{\frac{B}{\bar{T}}} - \bar{q}_a \right) \text{(II)} \dots (2). \\
 & + V' \left(\frac{\epsilon}{p} A e^{\frac{B}{\bar{T}}} \cdot \frac{BT'}{\bar{T}^2} - \bar{q}'_a \right) \text{(III)} \\
 & + R_{LHF} \text{(IV)}
 \end{aligned}$$

Term I stands for the combined effects from SST anomalies and air humidity. Term II is for the impacts of intraseasonal surface wind anomalies. Term III denotes the impacts on LHF due to nonlinear interactions between intraseasonal SST and intraseasonal wind anomalies. R_{LHF} (Term IV) denotes the residual term.

To capture the development of equatorial convections, the moist static energy (MSE) and the MSE budget are also utilized. MSE is usually used as a proxy for atmosphere convections (Kiranmayi and Maloney, 2011). It is defined as $m = C_p T_a + gz + L_v q$ where m is for MSE, C_p is the specific heat at constant pressure, T_a is the air temperature, g is the gravitational constant, z is the height above the surface, and q is the specific humidity. The intraseasonal MSE budget is written as (Maloney, 2009; Kiranmayi and Maloney, 2011)

$$\frac{\partial \langle m \rangle'}{\partial t} = H'_{adv} + V'_{adv} + LW' + SW' + LHF' + SHF' + R_{MSE} \dots (3),$$

where m denotes MSE; $\langle \rangle = \int_{1000}^{100} dp$ denotes the vertical integral from 1,000 hPa to 100 hPa; $H_{adv} = -\langle \vec{V}_H \cdot \nabla m \rangle$ is the horizontal advection, and \vec{V}_H is the horizontal wind velocity; $V_{adv} = -\langle \omega \frac{\partial m}{\partial p} \rangle$ is the vertical advection, and ω is the vertical velocity; the vertically integrated longwave radiation (LW) and shortwave radiation (SW) are calculated as the differences of net fluxes between the top of the atmosphere and the sea surface; and R_{MSE} is the residual term.

The components of the involved variables are obtained by the Butterworth filter. The intraseasonal signals are applied with a 20–100-day band-pass filter, the background components are obtained by a 100-day low-pass filter. In order to show the key phenomena of the ocean–atmosphere interaction, the composite analysis is used, and all the intraseasonal signals are averaged with respect to the selected intraseasonal events. Pattern correlation is employed to diagnose the linear relation between two spatial patterns (Clodman, 1987; Lee and Kim, 2012; Zou and Zhou, 2016). The model fidelity of northward propagation is quantified by the pattern correlation coefficient (PCC) between CMIP6 simulation and observation (Li et al., 2021). The statistical significances of both PCC and the composite analysis are tested with the Student's t-test. The effective number of degrees of freedom is determined following the modified Chelton method (Pyper and Peterman, 1998).

3 RESULTS

3.1 Biases of CMIP6 Model Simulations

The biases for precipitation are still obvious in the 6th Coupled Model Inter-comparison Project (CMIP6; Eyring et al., 2016). The simulated intraseasonal variance of monsoon precipitation is smaller than the observation in most models. The standard deviation (STD) of intraseasonal rainfall anomalies in 14 out of total 20 CMIP6 models is lower than 12 mm/day (Figures 1C, F–L, P–U), while the observed rainfall STD reach up to 21 mm/day (Figure 1A). Thus, for 70% of the CMIP6 models, the intraseasonal rainfall anomalies are around half of the observation.

Correspondingly, the model biases are also clear in the ocean–atmosphere interaction, for example, over the SEIO. Statistically, the oceanic impacts on the atmosphere can be simply quantified with the correlation between the SST anomalies and the sum of latent heat flux (LHF) and sensible heat flux (SHF; Cayan, 1992; Xi et al., 2015). For example, according to Xi et al. (2015) and Vialard et al. (2008), when there is a positive correlation between SST anomalies and the sum of LHF and SHF anomalies, the ocean drives the atmosphere. In the CMIP6 models in which the daily variables (SST, LHF, SHF, and precipitation) are available, such correlations during ISM (from June to September) at intraseasonal timescales are

shown in Figure 2. Compared with observations (Figure 2A), pronounced differences occur over the southeastern Indian Ocean (SEIO) within 75°E–95°E and 15°S–5°S. In nature, the significant correlation coefficients larger than 0.6 indicate that the ocean plays an active role during ISM. In contrast, the correlation coefficients between intraseasonal SST anomalies and the intraseasonal SHF + LHF in CMIP6 models are generally smaller than 0.2 and are not statistically significant (Figures 2B–U).

The bias of model simulations calls for further exploration on the ocean–atmosphere interaction over the southeastern Indian Ocean (SEIO) and the associated connection with the monsoon rainfall.

3.2 Local Intraseasonal SST Impacts Over SEIO

The standard deviations (STDs) of intraseasonal SST anomalies are shown in Figure 3. They are pronounced over the SEIO during boreal summer (June–September, JJAS; Li et al., 2008; Vinayachandran and Saji, 2008; Liang et al., 2018). The region (75°E–95°E and 15°S–5°S, black box in Figures 2A, 3) with an active oceanic impact and a large variance of intraseasonal SST anomalies is selected. The regional mean intraseasonal SST anomalies over 75°E–95°E and 15°S–5°S are shown in Figure 4. They are used as a reference for the following composite analysis. The days, when the regional mean SST anomalies over the black box (Figure 2A) reach the local maximum and are larger than the STD of the reference, are regarded as the day 0 of the warm SST events. There are a total of 62 events from 1985 to 2014 (red circles in Figure 4).

The composite intraseasonal SST, LHF, and surface wind anomalies averaged on day 0 are shown in Figure 5A. On day 0, warm SST anomalies reach 0.3°C over SEIO, and the LHF is reinforced due to warm SST anomalies, as shown with the black contours in Figure 5A. The composite regional mean LHF over SEIO (15°S–5°S and 75–95°E, black box in Figure 3) and the decomposition following Eq. (2) are shown in Figure 6A. Starting from day –8, warm SST anomalies occur over SEIO (yellow curve in Figure 6C), and LHF increases accordingly (Term I and yellow line in Figure 6A). Around day 0, the enhancement of LHF due to Term I reaches the maximum since the SST anomalies reach the maximum (yellow curve in Figure 6C). Generally, Term I consists of two parts [refer to Eq. (3)], the SST effects on LHF $\left(Term_{SST} = \rho_0 C_d L_v \bar{V} \cdot \frac{\epsilon}{p} A e^{-\frac{B}{T}} \cdot \frac{BT'}{T^2} \right)$ and the near-surface air humidity on LHF $\left(Term_a = \rho_0 C_d L_v \bar{V} q'_a \right)$. The variation of both two terms are shown in Figure 6C. However, it is clear that SST effects play a dominant role (dark blue curve in Figure 6C) over SEIO, and $Term_{SST}$ can reach up to 10 W/m², while the associated $Term_a$ is confined within ± 2 W/m². After day 0, the warm SST anomalies reduce, and the oceanic contribution to the LHF also diminishes.

However, the increase in LHF does not terminate. Instead, it is boosted by the increase in surface winds. Around day 0, southeasterly wind anomalies begin to grow over the warm SST anomalies (arrows in Figure 5A). The southeasterly wind

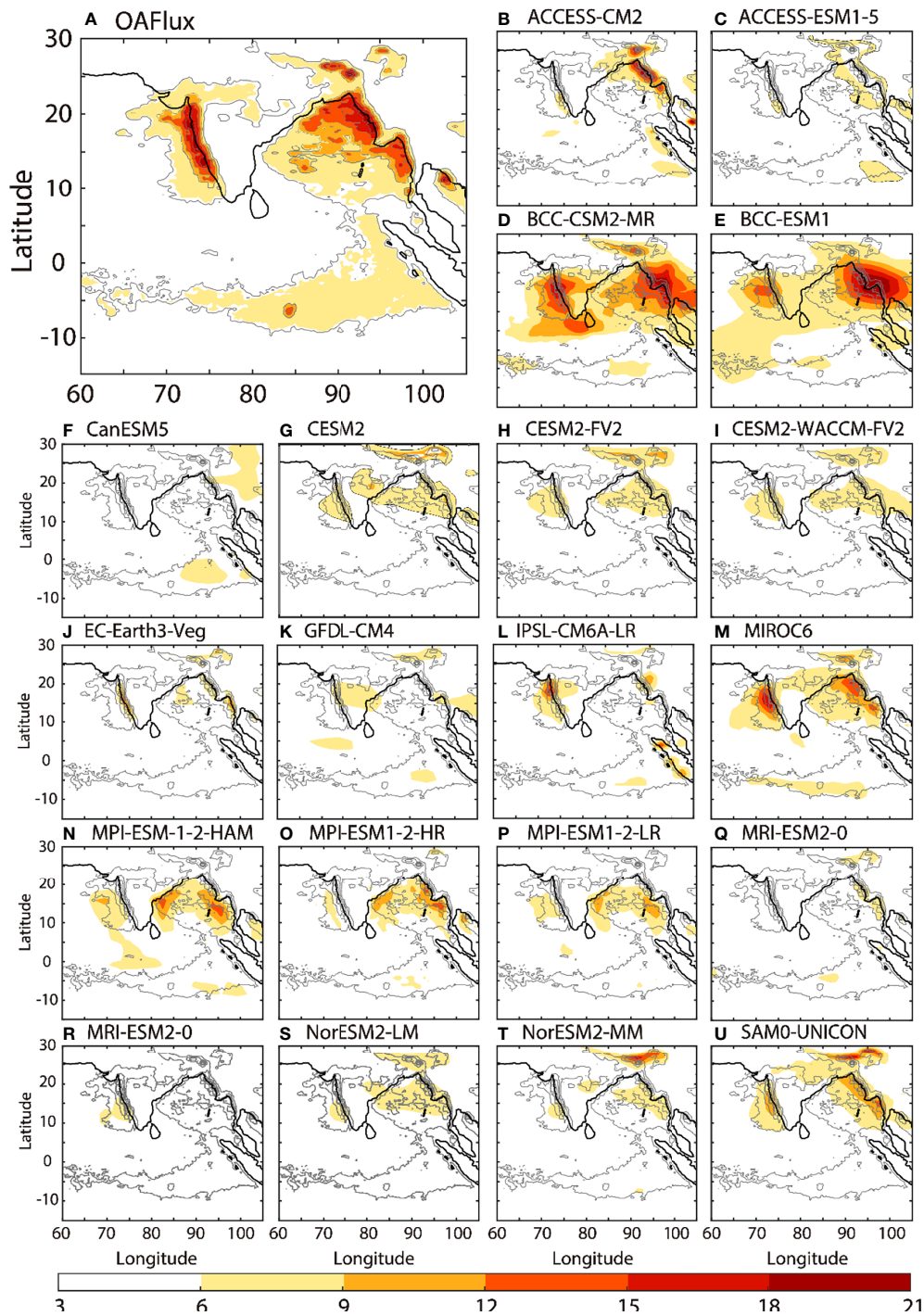


FIGURE 1 | Intraseasonal standard deviation (STD) of precipitation (unit: mm/day) during JJAS: **(A)** TRMM, **(B–U)** CMIP6 outputs. The gray contours are TRMM STD from 6 to 18 mm/day with an interval of 3 mm/day.

anomalies enhance the total winds, since the background winds are also southeasterly over SEIO (arrows in **Figure 3A**). The influences of warm SST anomalies on accelerating the low-level winds are common during ocean–atmosphere interactions. According to Chelton et al. (2001); Xie (2004), and Small et al. (2008), the SST modifications are responsible for increasing

instability and enhancing vertical mixing in the atmospheric boundary layer, which transport momentum from the upper boundary layer to the sea surface, and finally, the surface wind speed increases (Hayes et al., 1989; Maloney and Chelton, 2006; Chelton et al., 2007 and so on). The increment of surface wind speed gives rise to the positive anomalies of latent heat flux

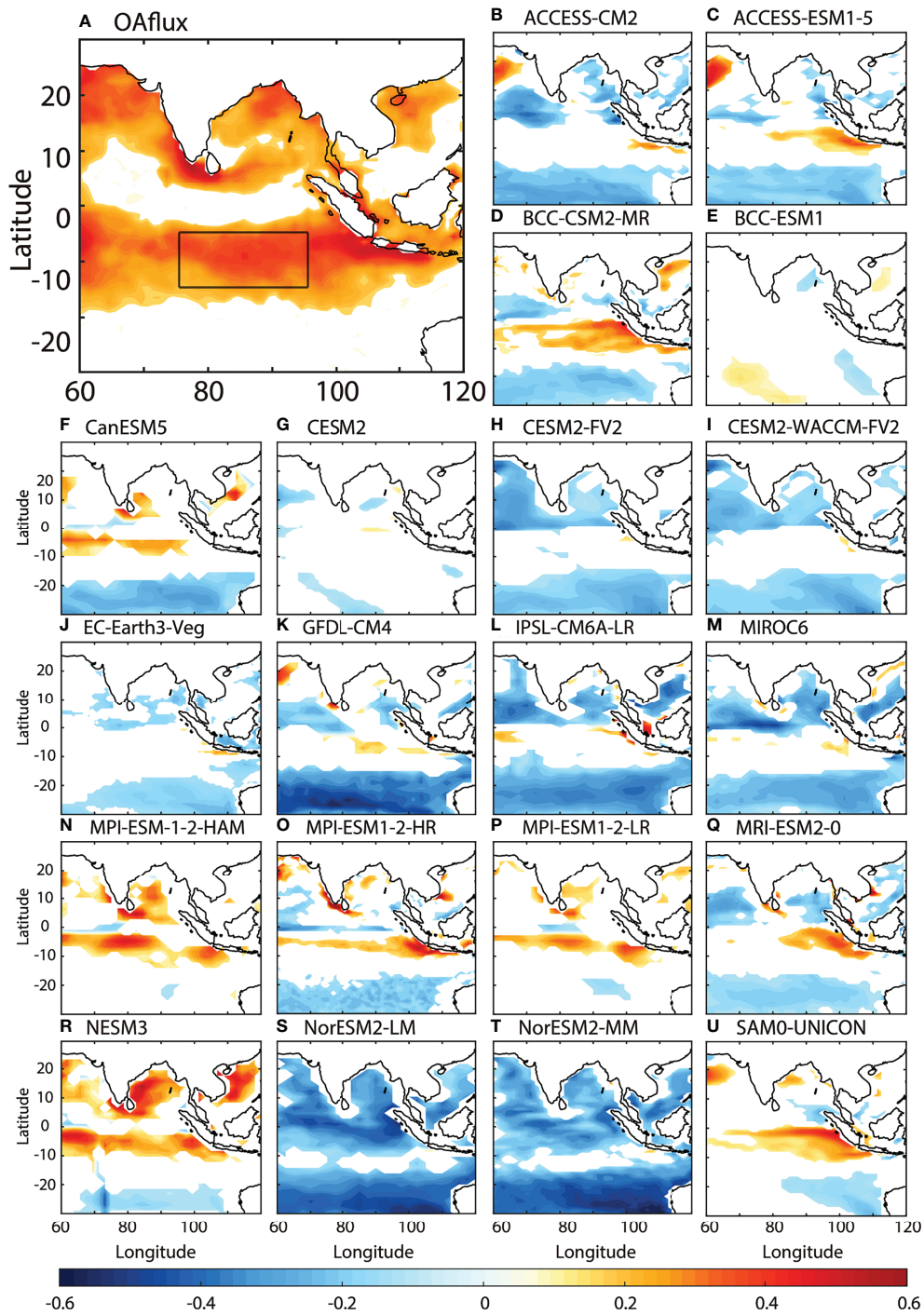


FIGURE 2 | Ocean–atmosphere interactions at intraseasonal time scales during JJAS. Colors are the intraseasonal correlations between SST and LHF+SHF in (A) OAF flux and (B–U) CMIP6 outputs. All signals are statistically significant at a 95% confidence level. The black box in Figure 1A denotes the region with pronounced air–se interaction in the southeastern Indian Ocean (SEIO, 75°E–95°E, 15°S–5°S).

around day 0 over SEIO (Term II, red line in Figure 6A), which agrees with the positive wind–evaporation–SST (WES) feedback (Neelin et al., 1987; Xie and Philander, 1994). Consistently, the total latent flux keeps growing on day 4 over SEIO (blue line in

Figure 6A), although the area with warm SST anomalies shrinks (yellow line in Figure 6B). In the decomposition of LHF, the influences from other terms are not strong. For instance, in Figure 6A, the interaction between the intraseasonal SST and

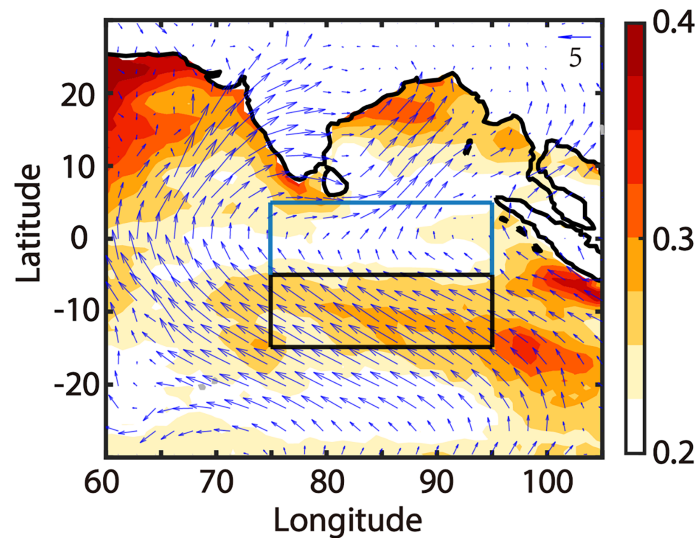
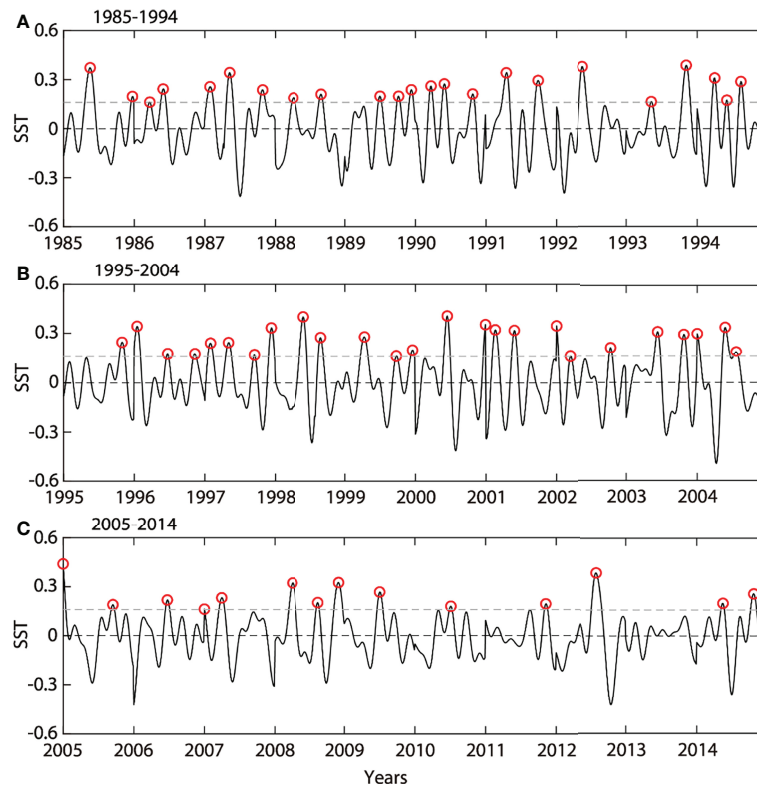


FIGURE 3 | The STD of intraseasonal SST anomalies (colors, unit: °C) and climatological surface wind vectors during boreal summer (arrows, unit: m/s). The black box is the same as the black box in **Figure 1A** (75°E–95°E, 15°S–5°S), over which one can also see the pronounced variation of intraseasonal SST anomalies. The blue one is the region in the equatorial Indian Ocean (EIO, 75°E–95°E, 5°S–5°N).

intraseasonal winds is small [Term III in Eq. (2) and purple line in **Figure 6A**]. The residual term in Eq. (2) is also small [R_{LHF} in Eq. (2) and green line in **Figure 6A**].

The warm intraseasonal SST anomalies are constrained over the SEIO. However, the consequent southeasterly wind

anomalies extend from the SEIO to the deep tropics. As shown in **Figure 5B**, southeasterly wind anomalies prevail over SEIO. On day 4, the LHF propagates equatorward along with the surface winds, although the warm SST anomalies reduce over SEIO and have no evidence of propagating northward. The



Q29 **FIGURE 4** | Intraseasonal SST (black curves, unit: °C) anomalies averaged within 75°E–95°E and 15°S–5°S during ISM (June–September) from OAF flux within 1985–1994 (A), 1995–2004 (B) and 1995–2014 (C).

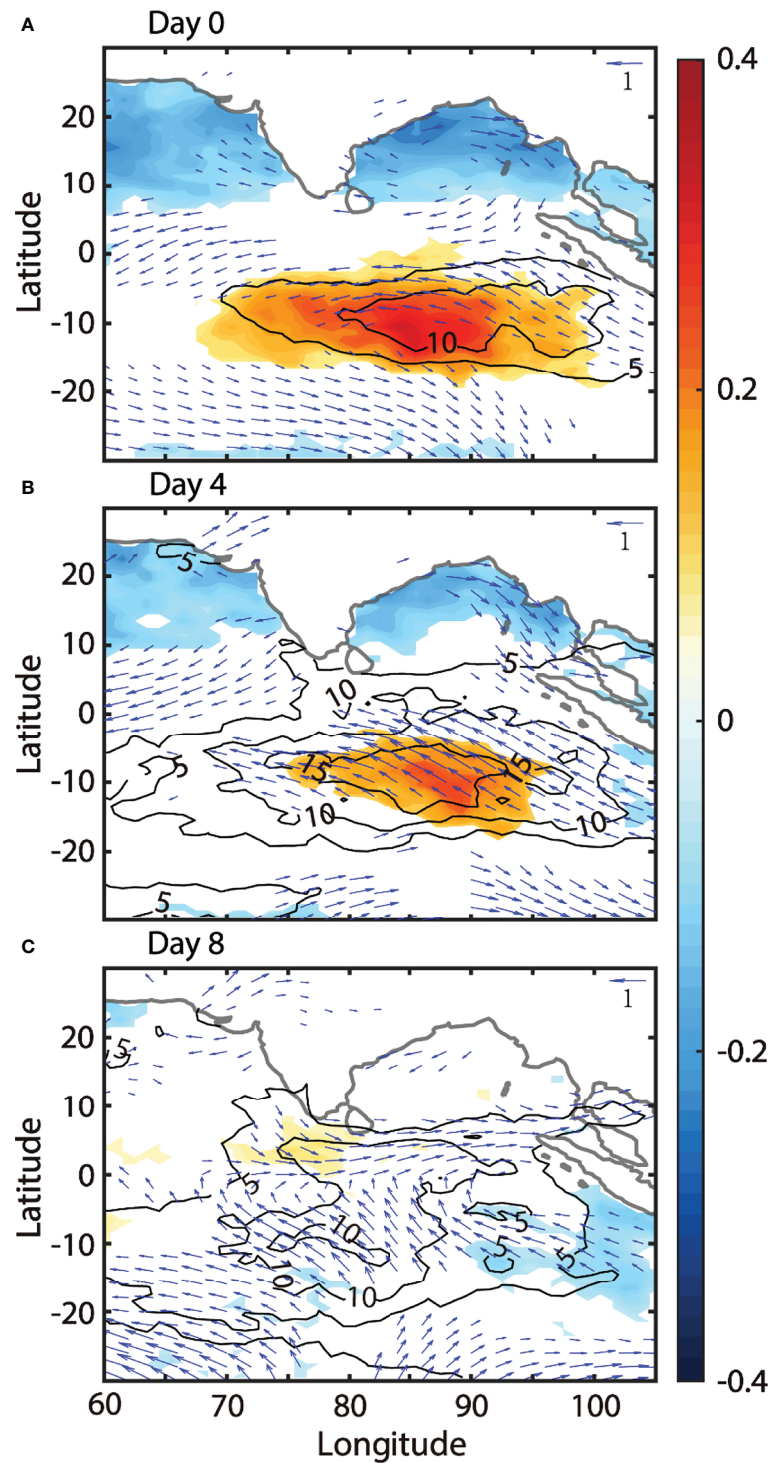


FIGURE 5 | The composite of intraseasonal SST (colors, unit: °C), LHF (black contours, unit: W/m²) and surface wind (blue arrows, unit: m/s) anomalies on Days 0 (A), 4 (B), and 8 (C).

equatorward propagations of surface wind anomalies and LHF reach the equator around day 4, as the southerly component of surface wind anomalies and LHF at the values of 10 W/m² begin to occur over the equator on day 4 (contours and vectors

in **Figure 5B**). The signals of wind anomalies and LHF persist until day 8, as the southerly component of wind anomalies and larger LHF prevail within 0° to 5°N on day 8 (contours and vectors in **Figure 5C**). The decomposition of LHF in Eq. (2)

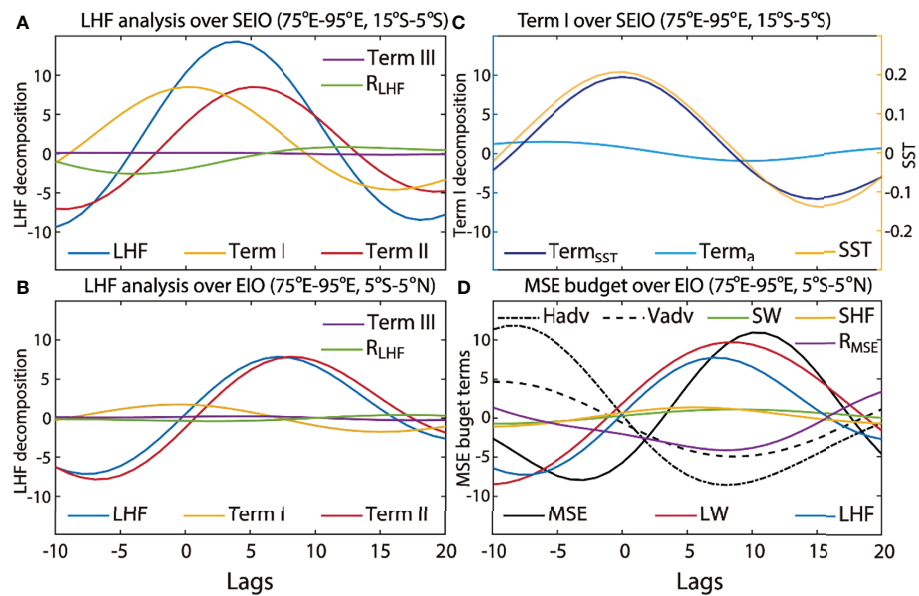


FIGURE 6 | (A) Decomposition of intraseasonal LHF (unit: W/m^2) averaged over SEIO. LHF is denoted with the blue curve. Term I (yellow curve) and Term II (red curve) denote the latent heat anomalies induced by SST anomalies and wind anomalies, respectively. Term III (purple curve) denotes the perturbations coming from both wind and SST anomalies. R_{LHF} (green curve) is the residual term. **(B)** is the same as **(A)**, but over Equatorial Indian Ocean (EIO, the blue box in **Figure 3**). **(C)** is the same as **(A)**, but for the decomposition of Term I (blue curves, unit: W/m^2) and intraseasonal SST anomalies (yellow curve, unit: $^{\circ}C$) over SEIO. In Eq. (3), Term I can be decomposed as the difference of $Term_{SST} = \rho_0 C_d L_v \bar{V} \cdot \frac{\epsilon}{p} A e^{\frac{B}{T}} \cdot \frac{BT'}{T^2}$ (dark blue curve) and $Term_a = \rho_0 C_d L_v \bar{V} q'_a$ (light blue curve). **(D)** Integrated MSE budget averaged within EIO. Black curve represents MSE (unit: $10^6 J/m^2$). Black dot-dashed curve represents the horizontal MSE advection; black dashed one represents the vertical MSE advection (unit: W/m^2). Red, green, blue, and yellow curves are longwave radiation, shortwave radiation, LHF, and SHF (unit: W/m^2), respectively. Purple curve is the residual term.

over the equatorial Indian Ocean (EIO, within $75^{\circ}E-95^{\circ}E$ and $5^{\circ}S-5^{\circ}N$; blue box in **Figure 3**) is shown in **Figure 6B**. The total LHF anomalies over EIO appear 3 days after that over SEIO and reach the local maximum around day 7 (blue line in **Figure 6B**). A key difference in the decomposition of the LHF between SEIO (**Figure 6A**) and EIO (**Figure 6B**) resides in the influence of SST anomalies. Warm SST anomalies over EIO are not significant (**Figure 5B**). Thus, their impact on the LHF is small [Term I in Eq. (2) and yellow line in **Figure 6B**]. In contrast, the southeasterly winds extend to the equatorial region, which plays a dominant role in the variation of LHF [Term II in Eq. (2) and red line in **Figure 6B**]. This is consistent with previous studies by Araligidad and Maloney (2008); Grodsky et al. (2009), and Gao et al. (2018) that, within the equatorial region, the variation in intraseasonal LHF is mainly attributable to atmospheric wind anomalies rather than to the oceanic thermal effects.

3.3 The Enhanced Equatorial Atmospheric Convection

Over EIO ($75^{\circ}E-95^{\circ}E$, $5^{\circ}S-5^{\circ}N$), the atmosphere becomes unstable due to the enhanced LHF. The moist static energy (MSE) is usually a good proxy for the development of atmospheric convection (Kiranmayi and Maloney, 2011). The budget of intraseasonal MSE is helpful for detecting the influential factors [see Eq. (3); Maloney, 2009; Kiranmayi and Maloney,

2011]. **Figure 6D** shows the regional mean of each term in Eq. (3) over $75^{\circ}E-95^{\circ}E$ and $5^{\circ}S-5^{\circ}N$. The column-integrated MSE (black solid curve) over the deep tropics reaches the maximum around day 10, which denotes the mature phase of the equatorial convection. During the growth of MSE from day 0 to day 10, the effects from longwave radiation (LW, red curve in **Figure 6D**) and LHF (blue curve in **Figure 6D**) are obvious, and they play dominant roles. LW plays a primary role and denotes the contribution of longwave heating during the atmospheric cumulus convective development (Kiranmayi & Maloney, 2011). LHF also plays an important role, which is associated with the contribution of intraseasonal wind anomalies from the sea surface. The other components, such as the horizontal (black dot dashed curve in **Figure 6D**) and vertical (black dashed curve in **Figure 6D**) advection are moderate from day 0 to day 10. The shortwave radiation (SW, green curve in **Figure 6D**) and SHF (yellow curve in **Figure 6D**) are tiny. The dominant roles of LW and LHF over tropical Indian Ocean are also consistent with other MSE budget analyses during the period of MJO during boreal winter (DeMott et al., 2016) and MISO/BSISO in the boreal summer (Gao et al., 2018). Moreover, in this study, the enhancement of LHF is attributable to the warm SST anomalies over SEIO. The intraseasonal oceanic effects on the atmosphere are not confined locally in SEIO. Instead, they are transported by the wind anomalies and support the atmospheric convection in the deep tropics.

3.4 Cross-Equatorial Influence on the ISM Rainfall

The equatorial convection triggered by the enhanced LHF propagates northward as MISO during boreal summer, which is an important trigger of intraseasonal variabilities over the Indian subcontinent (Karmakar and Krishnamurti, 2018; Qin et al., 2020; Qin et al., 2021; Li et al., 2022a). In **Figure 7A**, the Hovmöller diagrams of observed LHF (contours) and satellite-based rainfall (colors) anomalies during active convection are shown with respect to day 0. To match up with the time domain of TRMM dataset, the day 0s are obtained within 1998–2014 (red circles in **Figure 4**). Noteworthy, these involved day 0s (or cases) are not those events selected by the pronounced

intraseasonal variabilities in the monsoon region (e.g., the intraseasonal rainfall anomalies over Bay of Bengal, Li et al., 2022b; Zhou et al., 2017a), which were commonly used in many previous studies (Suhass et al., 2012; Girishkumar et al., 2017). One can see that the northward propagations of LHF and precipitation from the equator to the monsoon region are closely related to the intraseasonal warm SST anomalies over SEIO (**Figure 7A**). As mentioned before, positive LHF anomalies (contours) occur around the peak of warm SST anomalies over SEIO (day 0) and then spread northwestward to the equator. The equatorward intraseasonal wind anomalies along with LHF reach the equator and support the development of equatorial convection (colors) around day 10. Under the

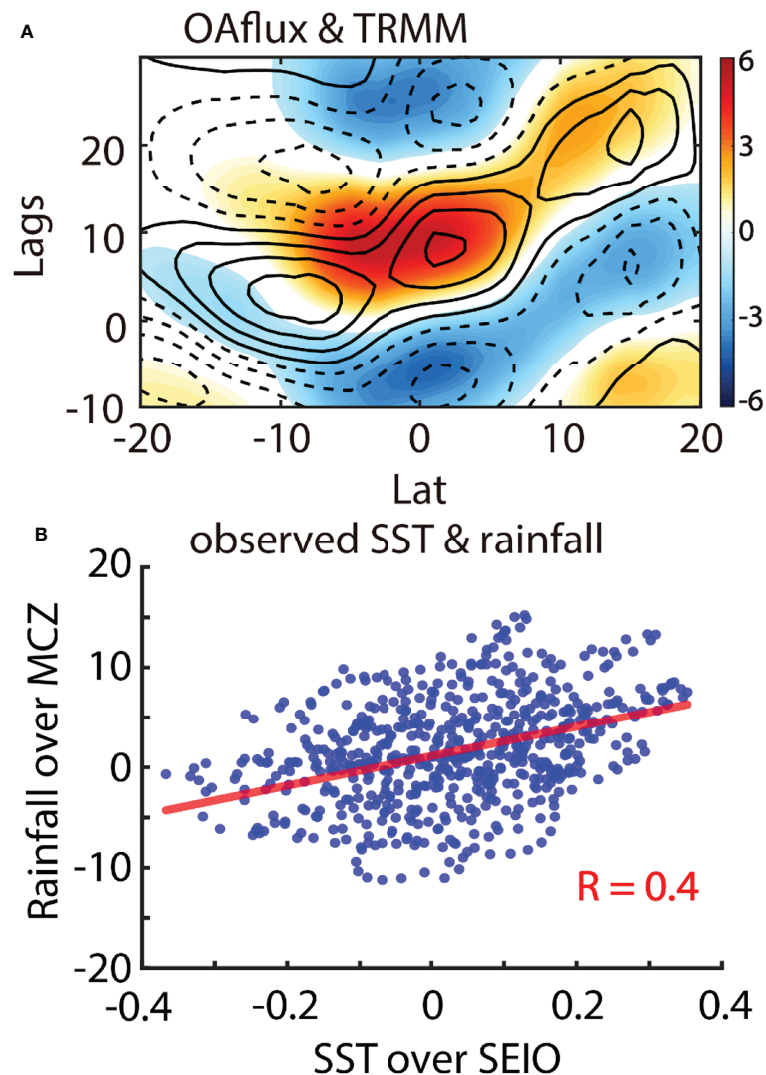
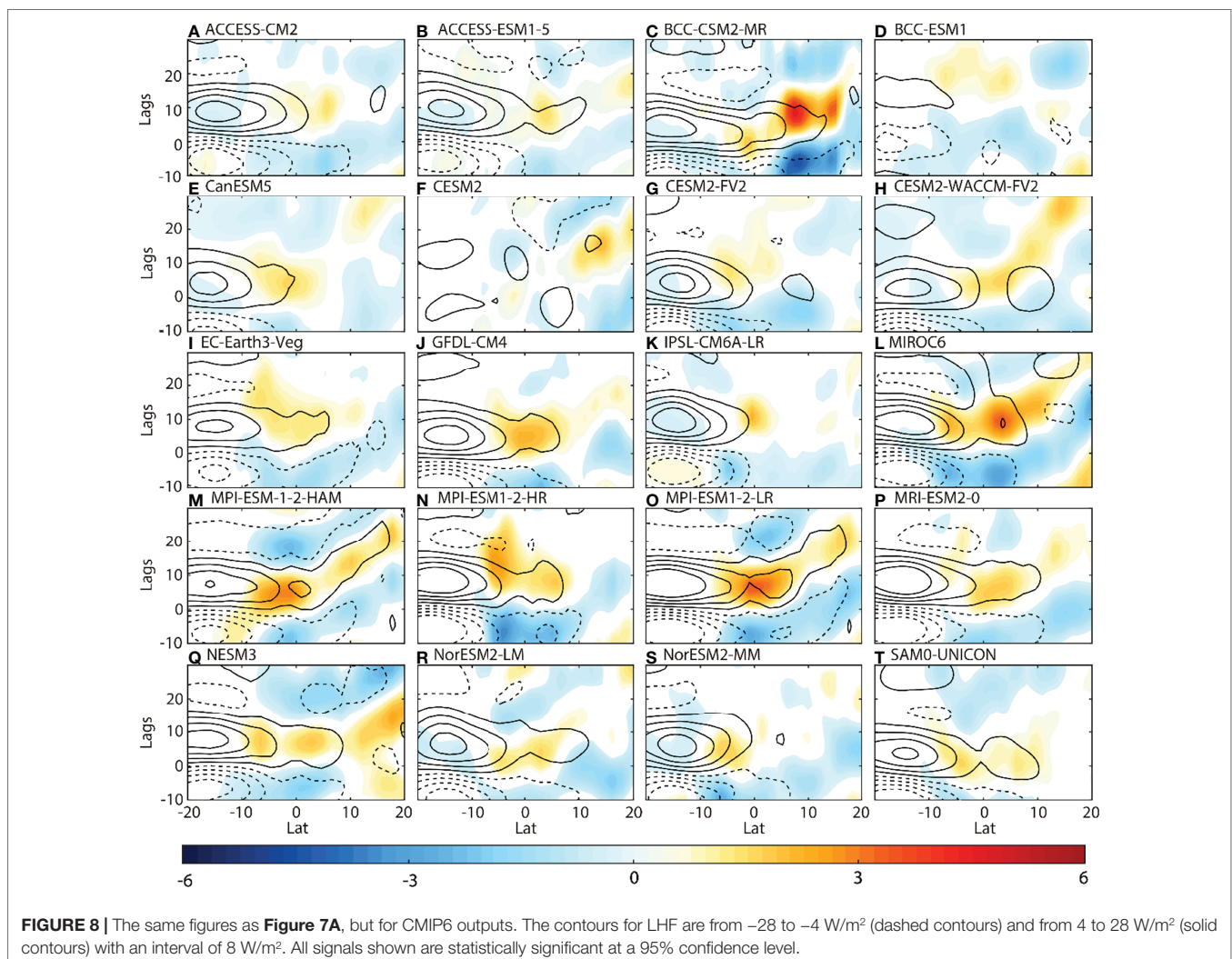


FIGURE 7 | (A) Composite Hovmöller diagrams of intraseasonal rainfall (colors, unit: mm/day) and LHF (contours, unit: W/m^2) anomalies averaged within $75^{\circ}E$ – $95^{\circ}E$. LHF from OaFlux and rainfall from TRMM. The dashed contours for LHF are from -12 to -4 W/m^2 , and the solid contours are from 4 to 16 W/m^2 . The interval is 4 W/m^2 . **(B)** The relationship between the intraseasonal SST anomalies over SEIO and the intraseasonal rainfall over MCZ ($75^{\circ}E$ – $95^{\circ}E$, $10^{\circ}N$ – $20^{\circ}N$). The blue dots are obtained from the observed cases during 1998–2014 (red circles in **Figure 4**). For each case, the intraseasonal SST anomalies from Day -10 to Day 10 are shown along the x-axis. The y-value of each blue dots is the corresponding intraseasonal rainfall in MCZ after 20 days (Days 10–30). The red line is estimated by the least square fit, and the correlation coefficient is statistically significant at a confidence level of 95%.

support of easterly vertical wind shear (Jiang et al., 2004) and atmospheric meridional advection (Bellon and Sobel, 2008), the enhanced tropical convection spreads northward as MISO and positive rainfall anomalies are induced over the monsoon region.

Statistically, the variation of the intraseasonal rainfall anomalies over the monsoon core zone (MCZ, 75°E–95°E, 10°N–20°N) in the Northern Hemisphere also has a positive correlation with that of the warm SST anomalies over SEIO in the Southern Hemisphere. In **Figure 7B**, the blue dots are obtained from the intraseasonal events during 1998–2014, which are the same as those in the composite of **Figure 7A**. For each case, the variation of the intraseasonal SST anomalies from day –10 to day 10 are shown as the x-values of the blue dots. The y-values are the corresponding intraseasonal rainfall in MCZ after 20 days (days 10–30). In total, there are 31 cases and 651 blue dots in **Figure 7B**. The red line is estimated by the least square fit, and the correlation coefficient is 0.4, which is statistically significant at a confidence level of 95%.

The correlation coefficient of 0.4 indicates that the above cross-equatorial process is not a predominant contributor but is inevitable to the monsoon rainfall events. The above correlation coefficient is not as high as the ones obtained from the traditional monsoon modes (Lee et al., 2012; Suhas et al., 2012; Zhou et al., 2017a). For example, a recent Central Indian Ocean (CIO) mode is apt at capturing the northward propagation and has a high correlation with the monsoon rainfall over the Bay of Bengal (Zhou et al., 2017a; Zhou et al., 2017b; Qin et al., 2021). The value of 0.4 for the cross-hemisphere implies that the relation between SEIO and MCZ is not the one-to-one correspondence as the above tradition ones. In other words, the cross-hemispheric impact from SEIO on MCZ is not the most dominant mechanism for the monsoon rainfall events. Instead, it is a good complement to the recent widely accepted mechanisms for MISO like vertical shear of easterly wind (Jiang et al., 2004) and atmospheric meridional advection (Bellon and Sobel, 2008) and can help to ameliorate the urgent need of the recent climate models that shows a clear bias of monsoon rainfall (**Figure 1**).



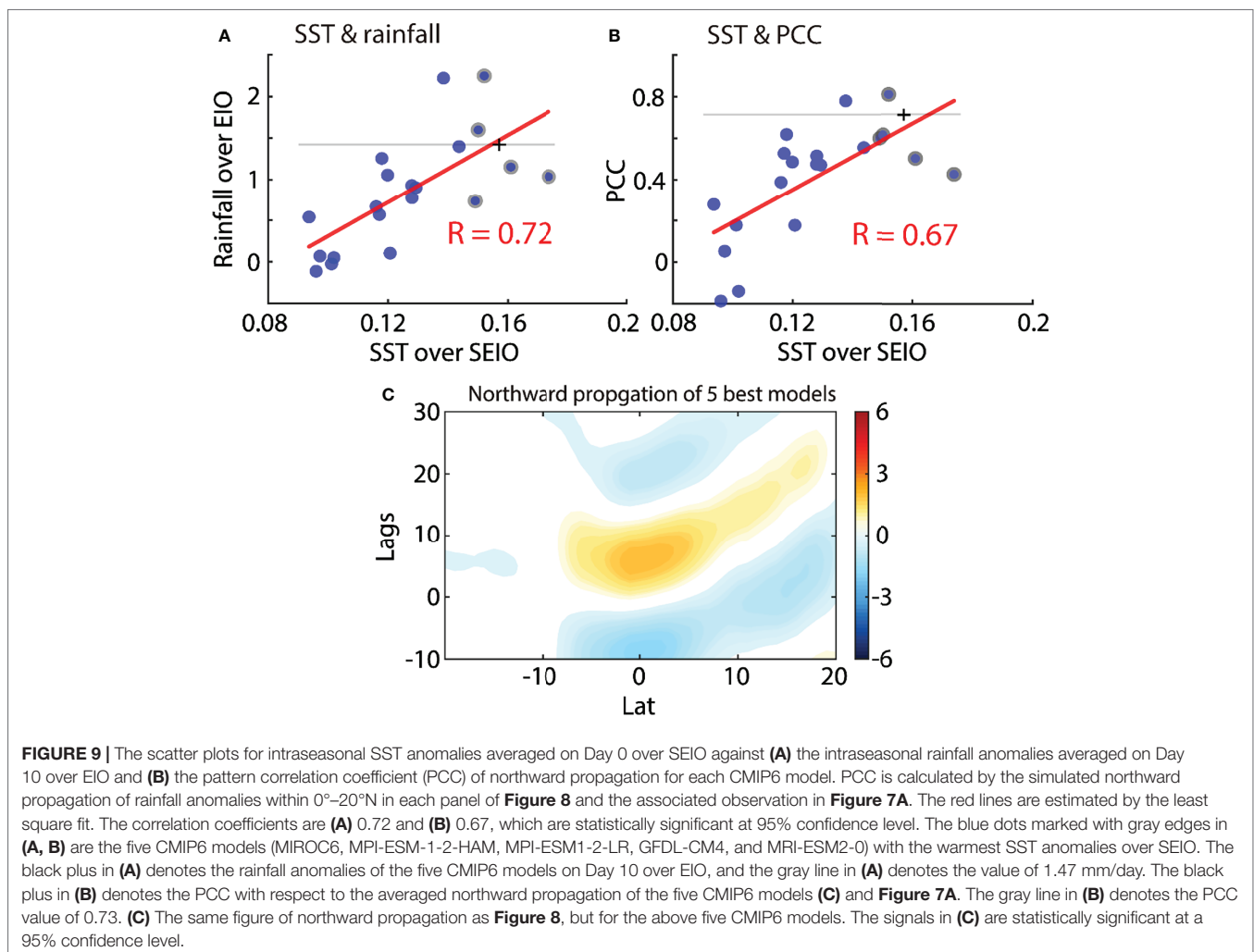
3.5 The Bias of CMIP6 and Probable Reason

The performance of CMIP6 can be checked in **Figure 8**, which is a similar Hovmöller diagram as in **Figure 7A**. The warm SST events over SEIO are obtained separately in each CMIP6 output following the routes described in **Figure 4**. The case numbers of each CMIP6 model within 1985–2014 are shown in **Table 1**. The numbers of the simulated cases are close to the observed one.

Obviously, in CMIP6, the northward propagations from the equator to the monsoon region are not well simulated, especially the intensity (colors in **Figure 8**). Compared to the observation, the intensities of northward propagations in nearly all the CMIP6 are much weaker or even insignificant. The observed northward propagation starts from the equator around day 10 (reddish in **Figure 7A**). At the initial stage of MISO, the observed equatorial rainfall anomalies are ~ 5 mm/day. In contrast, all the CMIP6 simulations are only 1–3 mm/day (reddish in **Figure 8**), which is only half of the observations. That the simulated tropical rainfall in CMIP6 is weaker than the observations is partially attributable to the bias in the above air–sea interactions over SEIO. In reality, strong equatorial convections are nourished by the equatorward

LHF anomalies originating from SEIO. However, in CMIP6 (**Figure 8**), LHF anomalies are trapped over the southern Indian Ocean (20°S – 0°) from day 0 to day 15, and they do not propagate equatorward (contours in **Figure 8**). As a result, the deep tropics lack energy for convection in simulations, which also explains why the CMIP6 models yield small STD of intraseasonal rainfall anomalies around the equator (**Figures 1B–U**).

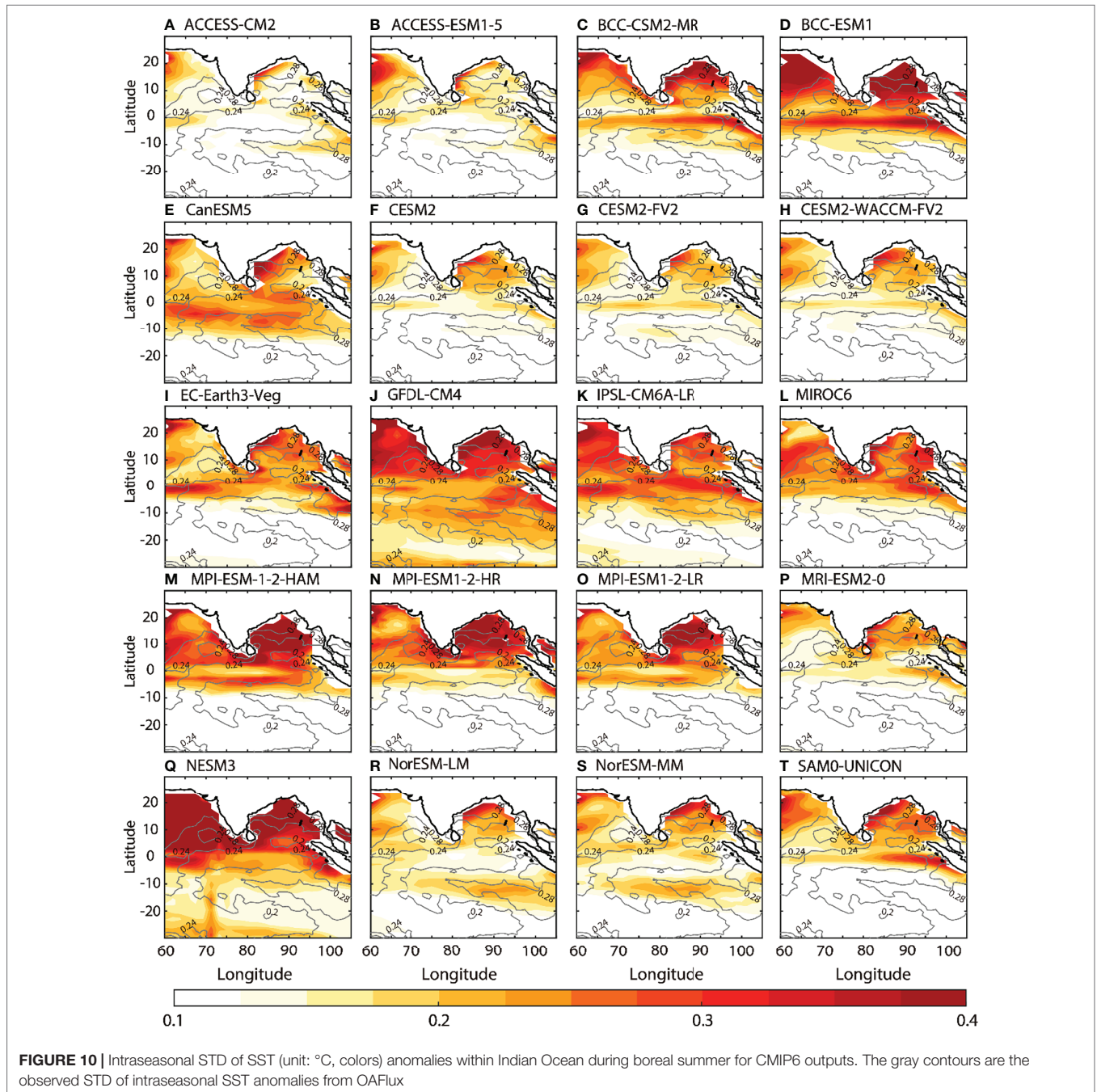
Despite the systematic deficient simulations over SEIO in CMIP6, results still show the importance of ocean–atmosphere interaction over SEIO on the equatorial rainfall anomalies and the northward propagation. The relationship between simulated SST anomalies over SEIO and simulated rainfall anomalies over EIO is shown in **Figure 9A**. Each blue dot in **Figure 9A** represents one of the CMIP6 model outputs. The x-value of a blue dot is the warm SST anomaly averaged over SEIO and on day 0 of all the selected events in each CMIP6 model (**Table 1**). The y-value is the rainfall anomaly averaged over EIO and on day 10, correspondingly. The linear regression is shown with a red line, and the correlation coefficient is 0.72, which is statistically significant at a confidence level of 95%. It denotes that stronger ocean–atmosphere interactions over SEIO are favorable for



larger equatorial rainfall anomalies in CMIP6 models. On the other hand, when the equatorial rainfall anomalies are well simulated, the simulated northward propagation will become more realistic. The relationship between SST anomalies over SEIO and northward propagation is shown in **Figure 9B**. Here, the northward propagation is quantified as the pattern correlation coefficient (PCC) between the northward propagation of each CMIP6 model and the observation (Clodman, 1987). Specifically, the calculation of PCC is based on the northward propagation of rainfall anomalies within 0°–20°N in each panel of **Figure 8** and the associated observation in **Figure 7A**. It is clear that there is a

positive correlation between SST anomalies over SEIO and PCC, and the significant correlation coefficient is 0.67.

In this way, if the model simulations can provide a better simulation of SST anomalies over SEIO, the associated ocean-atmosphere interaction will prompt stronger equatorial convection and larger precipitation in 10 days, which will lead to more realistic northward propagation of ISVs and heavier summer rainfall over monsoon region. For example, the top 5 models with the warmest SST anomalies over SEIO can reproduce more realistic northward propagating MISOs, which exceeds at least 85% of the CMIP6 models. The five CMIP6 models are



MIROC6, MPI-ESM-1-2-HAM, MPI-ESM1-2-LR, GFDL-CM4, and MRI-ESM2-0 (the circles with gray edges in **Figures 9A, B**). The composite Hovmöller diagram of intraseasonal rainfall anomalies is shown in **Figure 9C**. Over EIO, the mean rainfall anomaly on day 10 is 1.47 mm/day (also see black plus in **Figure 9A**). It is also denoted as the gray line in **Figure 9A**. There are only 3 of 20 CMIP6 outputs exceeding the gray line. In other words, the averaged equatorial rainfall of the top 5 models is stronger than 85% of the total 20 CMIP6 results. With stronger equatorial convections, the northward propagation is closer to nature, too (**Figure 9C**). The PCC between **Figure 9C** and the observed northward propagation in **Figure 7A** is 0.73 (black plus and gray line in **Figure 9B**). In total, 18 of 20 blue dots are under the gray line. That is, the northward propagation of the best five models is more realistic than 90% of the total 20 CMIP6 models. Therefore, as for CMIP6 models, further attention on the ocean–atmosphere interaction over SEIO is of great importance for better simulations of monsoon rainfall.

4 CONCLUSIONS AND DISCUSSION

In contemporary climate models, the weak Indian summer monsoon rainfall is a common bias. Consistently, the simulated northward-propagating MISO and the tropical convection are also weaker in boreal summer (Ahn et al., 2017, also see **Figure 1**). It is shown in this study that the cross-equatorial influences originating from the warm SST anomalies over the SEIO are prone to strengthen the tropical convection and consequently the precipitation in the Indian monsoon region. Warm intraseasonal SST anomalies over SEIO support local enhancement of the intraseasonal southeasterly wind anomalies and the latent heat flux. The southeasterly wind anomalies propagate equatorward from the Southern Hemisphere, although the warm SST anomalies are constrained to SEIO. The total winds get reinforced, since the intraseasonal wind anomalies share the same direction as the background winds. Due to the WES feedback, the LHF increases from SEIO to the deep tropics, along with the equatorward propagation of wind anomalies. As a result, the MSE increases around the equator, and the tropical convection becomes stronger. During boreal summer, the enhanced tropical convections propagate northward and cause extreme rainfall events over monsoon regions. Current results indicate that the inter-hemispheric impacts are an inevitable contributor to the heavy rainfall during ISM in the subtropics in the Northern Hemisphere. However, such process understanding is not well captured in CMIP6 models, which is one reason for the less simulated ISM rainfall than observations.

The unsatisfactory simulations of CMIP6 are associated with the defective ocean–atmosphere interaction over SEIO (**Figure 2**). One clue is that the variances of intraseasonal

SST anomalies are feeble and far from the observations (**Figure 10**). The STD of simulated intraseasonal SST anomalies in most CMIP6 models is hardly larger than 0.15°C, which is about half of the observations. The weak SST anomalies are not powerful enough to drive the response in the low-level troposphere. As a result, the oceanic impact on the atmosphere cannot be captured in most CMIP6 models. However, most CMIP6 models do not provide oceanic variables, such as the 3-D temperature and currents. Thus, it is hard to apply a full heat budget analysis in the upper mixed layer and to detect the reasons dynamically. Moreover, there are many other reasons for the intraseasonal biases over SEIO, such as the geography of the southeastern Indian Ocean and the confluence of the Indian Ocean Dipole Mode (Saji et al., 1999; Murtugudde et al., 2000), South Equatorial Current and Indonesian Throughflow (Gordon et al., 1997; Murtugudde et al., 1998), the South Java Current (Quadfasel and Cresswell, 1992), and the feedbacks with Indonesian rainfall (Hendon, 2003). The complicated ocean environment increases the difficulty of a satisfactory simulation. The biases in climatological wind and SST over SEIO are other important concerns (Lee et al., 2013; Li et al., 2015), which are also possible reasons for weaker high-frequency signals like intraseasonal oscillations.

DATA AVAILABILITY STATEMENT

The original contributions presented in the study are included in the article/supplementary material. Further inquiries can be directed to the corresponding author.

AUTHOR CONTRIBUTIONS

ZM, LZ, JQ, and BL contributed to the conception and design of the study. All authors contributed to the article and approved the submitted version.

FUNDING

This work is supported by grants from National Natural Science Foundation of China (42076001 and 42106003).

ACKNOWLEDGMENTS

Constructive and valuable comments from the reviewers are greatly appreciated.

REFERENCES

- Ahn, M.-S., Kim, D., Sperber, K. R., Kang, I.-S., Maloney, E. D., Waliser, D. E., et al. (2017). MJO Simulation in CMIP5 Climate Models: MJO Skill Metrics and Process-Oriented Diagnosis. *Clim. Dyn.* 49, 4023–4045. doi: 10.1007/s00382-017-3558-4
- Ajayamohan, R. S. and Rao, S. A. (2008). Indian Ocean Dipole Modulates the Number of Extreme Rainfall Events Over India in a Warming Environment. *J. Meteorol. Soc Jpn.* 86, 245–252. doi: 10.2151/jmsj.86.245
- Araligidad, N. and Maloney, E. D. (2008). Wind-Driven Latent Heat Flux and the Intraseasonal Oscillation. *Geophys. Res. Lett.* 35, 317–333. doi: 10.1029/2007GL032746

- Ashok, K., Guan, Z., Saji, N. H. and Yamagata, T. (2004). Individual and Combined Influences of ENSO and the Indian Ocean Dipole on the Indian Summer Monsoon. *J. Clim.* 17, 3141–3155. doi: 10.1175/1520-0442(2004)017<3141:IAC IOE>2.0.CO;2
- Ashok, K., Guan, Z. and Yamagata, T. (2001). Impact of the Indian Ocean Dipole on the Relationship Between the Indian Monsoon Rainfall and ENSO. *Geophys. Res. Lett.* 28, 4499–4502. doi: 10.1029/2001GL013294
- Bellon, G. and Sobel, A. H. (2008). Poleward-Propagating Intraseasonal Monsoon Disturbances in an Intermediate-Complexity Axisymmetric Model. *J. Atmos. Sci.* 65, 470–489. doi: 10.1175/2007JAS2339.1
- Boos, W. R. and Kuang, Z. (2010). Mechanisms of Poleward Propagating, Intraseasonal Convective Anomalies in Cloud System-Resolving Models. *J. Atmos. Sci.* 67, 3673–3691. doi: 10.1175/2010JAS315.1
- Cayan, D. R. (1992). Variability of Latent and Sensible Heat Fluxes Estimated Using Bulk Formulae. *Atmosphere-Ocean* 30, 1–42. doi: 10.1080/07055900.1992.9649429
- Chelton, D. B., Esbensen, S. K., Schlax, M. G., Thum, N., Freilich, M. H., Wentz, F. J., et al. (2001). Observations of Coupling Between Surface Wind Stress and Sea Surface Temperature in the Eastern Tropical Pacific. *J. Clim.* 14, 1479–1498. doi: 10.1175/1520-0442(2001)014<1479:OOCBSW>2.0.CO;2
- Chelton, D., Schlax, M. G. and Samelson, R. M. (2007). Summertime Coupling Between Sea Surface Temperature and Wind Stress in the California Current System. *J. Phys. Oceanogr.* 37, 495–517. doi: 10.1175/JPO3025.1
- Clodman, S. (1987). Pattern Correlation Used to Forecast Mean Sea Level Pressure. *Mon. Weath. Rev.* 115, 1561–1574. doi: 10.1175/1520-0493(1987)115<1561:PCUTFM>2.0.CO;2
- DeMott, C. A., Benedict, J. J., Klingaman, N. P., Woolnough, S. J. and Randall, D. A. (2016). Diagnosing Ocean Feedbacks to the MJO: SST-Modulated Surface Fluxes and the Moist Static Energy Budget. *J. Geophys. Res. Atmos.* 121, 8350–8373. doi: 10.1002/2016JD025098
- DeMott, C. A., Stan, C. and Randall, D. A. (2013). Northward Propagation Mechanisms of the Boreal Summer Intraseasonal Oscillation in the ERA-Interim and SP-CCSM. *J. Clim.* 26, 1973–1992. doi: 10.1175/JCLI-D-12-00191.1
- Drbohlav, H.-K. L. and Wang, B. (2005). Mechanism of the Northward-Propagating Intraseasonal Oscillation: Insights From a Zonally Symmetric Model*. *J. Clim.* 18, 952–972. doi: 10.1175/JCLI3306.1
- Eyring, V., Bony, S., Meehl, G. A., Senior, C. A., Stevens, B., Stouffer, R. J., et al. (2016). Overview of the Coupled Model Intercomparison Project Phase 6 (CMIP6) Experimental Design and Organization. *Geosci. Model. Dev.* 9, 1937–1958. doi: 10.5194/gmd-9-1937-2016
- Fu, C. (2003). Potential Impacts of Human-Induced Land Cover Change on East Asia Monsoon. *Glob. Planet. Change* 37, 219–229. doi: 10.1016/S0921-8181(02)00207-2
- Fu, X. and Wang, B. (2004). Differences of Boreal Summer Intraseasonal Oscillations Simulated in an Atmosphere–Ocean Coupled Model and an Atmosphere-Only Model*. *J. Clim.* 17, 1263–1271. doi: 10.1175/1520-0442(2004)017<1263:DOBSIO>2.0.CO;2
- Fu, X., Wang, B., Li, T. and McCreary, J. P. (2003). Coupling Between Northward-Propagating, Intraseasonal Oscillations and Sea Surface Temperature in the Indian Ocean*. *J. Atmos. Sci.* 60, 1733–1753. doi: 10.1175/1520-0469(2003)060<1733:CBNIOA>2.0.CO;2
- Fu, X., Yang, B., Bao, Q. and Wang, B. (2008). Sea Surface Temperature Feedback Extends the Predictability of Tropical Intraseasonal Oscillation. *Mon. Weath. Rev.* 136, 577–597. doi: 10.1175/2007MWR2172.1
- Gao, Y., Klingaman, N. P., DeMott, C. A. and Hsu, P. (2018). Diagnosing Ocean Feedbacks to the BSISO: SST-Modulated Surface Fluxes and the Moist Static Energy Budget. *J. Geophys. Res. Atmos.*, 2018JD029303. doi: 10.1029/2018JD029303
- Gebregiorgis, D., Hathorne, E. C., Giosan, L., Clemens, S. C., Nürnberg, D. and Frank, M. (2018). Southern Hemisphere Forcing of South Asian Monsoon Precipitation Over the Past 1 Million Years. *Nat. Commun.* 9, 4702. doi: 10.1038/s41467-018-07076-2
- Girishkumar, M. S., Joseph, J., Thangaprakash, V. P., Pottapinjara, V. and McPhaden, M. J. (2017). Mixed Layer Temperature Budget for the Northward Propagating Summer Monsoon Intraseasonal Oscillation (MISO) in the Central Bay of Bengal. *J. Geophys. Res.* 122, 8841–8854. doi: 10.1002/2017JC013073
- Gordon, A. L., Ma, S., Olson, D. B., Hacker, P., Ffield, A., Talley, L. D., et al. (1997). Advection and Diffusion of Indonesian Throughflow Water Within the Indian Ocean South Equatorial Current. *Geophys. Res. Lett.* 24, 2573–2576. doi: 10.1029/97GL01061
- Goswami, B. N., Ajayamohan, R. S., Xavier, P. K. and Sengupta, D. (2003). Clustering of Synoptic Activity by Indian Summer Monsoon Intraseasonal Oscillations: Modulation Of Synoptic Activity By Iso. *Geophys. Res. Lett.* 30, 122–137. doi: 10.1029/2002GL016734
- Grodsky, S. A., Bentamy, A., Carton, J. and Pinker, R. T. (2009). Intraseasonal Latent Heat Flux Based on Satellite Observations. *J. Clim.* 22, 4539–4556. doi: 10.1175/2009JCLI2901.1
- Guan, Z., Ashok, K. and Yamagata, T. (2003). Summertime Response of the Tropical Atmosphere to the Indian Ocean Dipole Sea Surface Temperature Anomalies. *J. Meteorol. Soc Jpn.* 81, 533–561. doi: 10.2151/jmsj.81.533
- Hayes, S. P., McPhaden, M. J. and Wallace, J. M. (1989). The Influence of Sea-Surface Temperature on Surface Wind in the Eastern Equatorial Pacific: Weekly to Monthly Variability. *J. Clim.* 2, 1500–1506. doi: 10.1175/1520-0442(1989)002<1500:TIOST>2.0.CO;2
- Hendon, H. H. (2003). Indonesian Rainfall Variability: Impacts of ENSO and Local Air-Sea Interaction. *J. Clim.* 16, 1775–1790. doi: 10.1175/1520-0442(2003)016<1775:IRVIOE>2.0.CO;2
- Hendon, H. H. and Glick, J. (1997). Intraseasonal Air–Sea Interaction in the Tropical Indian and Pacific Oceans. *J. Clim.* 10, 647–661. doi: 10.1175/1520-0442(1997)010<0647:IASIIT>2.0.CO;2
- Hersbach, H., Bell, B., Berrisford, P., Hirahara, S., Horányi, A., Muñoz-Sabater, J., et al. (2020). The ERA5 Global Reanalysis. *Q. J. R. Meteorol. Soc.* 146, 1999–2049. doi: 10.1002/qj.3803
- Hu, W., Duan, A. and He, B. (2017). Evaluation of Intra-Seasonal Oscillation Simulations in IPCC AR5 Coupled GCMs Associated With the Asian Summer Monsoon. *Int. J. Climatol.* 37, 476–496. doi: 10.1002/joc.5016
- Hu, W., Duan, A. and Wu, G. (2015). Impact of Subdaily Air–Sea Interaction on Simulating Intraseasonal Oscillations Over the Tropical Asian Monsoon Region. *J. Clim.* 28, 1057–1073. doi: 10.1175/JCLI-D-14-00407.1
- Huffman, G. J., Bolvin, D. T., Nelkin, E. J., Wolff, D. B., Adler, R. F., Gu, G., et al. (2007). The TRMM Multisatellite Precipitation Analysis (TMPA): Quasi-Global, Multiyear, Combined-Sensor Precipitation Estimates at Fine Scales. *J. Hydrometeorol.* 8, 38–55. doi: 10.1175/JHM560.1
- Jiang, X., Li, T. and Wang, B. (2004). Structures and Mechanisms of the Northward Propagating Boreal Summer Intraseasonal Oscillation. *J. Clim.* 17, 1022–1039. doi: 10.1175/1520-0442(2004)017<1022:SAMOTN>2.0.CO;2
- Kang, I.-S., Kim, D. and Kug, J.-S. (2010). Mechanism for Northward Propagation of Boreal Summer Intraseasonal Oscillation: Convective Momentum Transport. *Geophys. Res. Lett.* 37, L24804. doi: 10.1029/2010GL045072
- Karmakar, N. and Krishnamurti, T. N. (2018). Characteristics of Northward Propagating Intraseasonal Oscillation in the Indian Summer Monsoon. *Clim. Dyn.* 52, 1903–1916. doi: 10.1007/s00382-018-4268-2
- Kemball-Cook, S. and Wang, B. (2001). Equatorial Waves and Air–Sea Interaction in the Boreal Summer Intraseasonal Oscillation. *J. Clim.* 14, 2923–2942. doi: 10.1175/1520-0442(2001)014<2923:EWAASI>2.0.CO;2
- Kemball-Cook, S., Wang, B. and Fu, X. (2001). Simulation of the Intraseasonal Oscillation in the ECHAM-4 Model: The Impact of Coupling With an Ocean Model*. *J. Atmos. Sci.* 59, 1433–1453. doi: 10.1175/1520-0469(2002)059<1433:SOTIOI>2.0.CO;2
- Kiranmayi, L. and Maloney, E. D. (2011). Intraseasonal Moist Static Energy Budget in Reanalysis Data. *J. Geophys. Res.* 116. doi: 10.1029/2011JD016031
- Lee, J.-J. and Kim, C. (2012). Roles of Surface Wind, NDVI and Snow Cover in the Recent Changes in Asian Dust Storm Occurrence Frequency. *Atmos. Environ.* 59, 366–375. doi: 10.1016/j.atmosenv.2012.05.022
- Lee, T., Waliser, D. E., Li, J.-L. F., Landerer, F. W. and Gierach, M. M. (2013). Evaluation of CMIP3 and CMIP5 Wind Stress Climatology Using Satellite Measurements and Atmospheric Reanalysis Products. *J. Clim.* 26, 5810–5826. doi: 10.1175/JCLI-D-12-00591.1
- Lee, J.-Y., Wang, B., Wheeler, M. C., Fu, X., Waliser, D. E. and Kang, I.-S. (2012). Real-Time Multivariate Indices for the Boreal Summer Intraseasonal Oscillation Over the Asian Summer Monsoon Region. *Clim. Dyn.* 40, 493–509. doi: 10.1007/s00382-012-1544-4
- Liang, Y.-C., Du, Y., Zhang, L., Zheng, X.-T. and Qiu, S. (2018). The 30-50-Day Intraseasonal Oscillation of SST and Precipitation in the South Tropical Indian Ocean. *Atmosphere* 9, 69. doi: 10.3390/atmos9020069

- Lin, J., Weickman, K. M., Kiladis, G. N., Mapes, B. E., Schubert, S., Suárez, M. J., et al. (2008). Subseasonal Variability Associated With Asian Summer Monsoon Simulated by 14 IPCC AR4 Coupled GCMs. *J. Clim.* 21, 4541–4567. doi: 10.1175/2008JCLI1816.1
- Li, T., Tam, F., Fu, X., Tianjun, Z. and Weijun, Z. (2008). Causes of the Intraseasonal SST Variability in the Tropical Indian Ocean. *Atmos. Ocean. Sci. Lett.* 1, 18–23. doi: 10.1080/16742834.2008.11446758
- Li, X., Tang, Y., Zhou, L., Yao, Z., Shen, Z., Li, J., et al. (2020b). Optimal Error Analysis of MJO Prediction Associated With Uncertainties in Sea Surface Temperature Over Indian Ocean. *Clim. Dyn.* 54, 4331–4350. doi: 10.1007/s00382-020-05230-5
- Liu, F., Wang, B. and Kang, I.-S. (2015). Roles of Barotropic Convective Momentum Transport in the Intraseasonal Oscillation. *J. Clim.* 28, 4908–4920. doi: 10.1175/JCLI-D-14-00575.1
- Li, G., Xie, S. and Du, Y. (2015). Monsoon-Induced Biases of Climate Models Over the Tropical Indian Ocean*. *J. Clim.* 28, 3058–3072. doi: 10.1175/JCLI-D-14-00740.1
- Li, B., Zhou, L., Qin, J. and Meng, Z. (2022a). Maintenance of Cyclonic Vortex During Monsoon Intraseasonal Oscillation: A View From Kinetic Energy Budget. *Geophys. Res. Lett.* 49, e2022GL097740. doi: 10.1029/2022GL097740
- Li, B., Zhou, L., Qin, J. and Meng, Z. (2022b). Key Process Diagnostics for Monsoon Intraseasonal Oscillation Over the Indian Ocean in Coupled CMIP6 Models. *Clim. Dyn.*, 1–18. doi: 10.1007/s00382-022-06245-w
- Li, B., Zhou, L., Qin, J. and Murtugudde, R. (2021). The Role of Vorticity Tilting in Northward-Propagating Monsoon Intraseasonal Oscillation. *Geophys. Res. Lett.* 48, e2021GL093304. doi: 10.1029/2021GL093304
- Li, B., Zhou, L., Wang, C., Gao, C., Qin, J. and Meng, Z. (2020a). Modulation of Tropical Cyclone Genesis in the Bay of Bengal by the Central Indian Ocean Mode. *J. Geophys. Res. Atmos.* 125. doi: 10.1029/2020JD032641
- Maloney, E. D. (2009). The Moist Static Energy Budget of a Composite Tropical Intraseasonal Oscillation in a Climate Model. *J. Clim.* 22, 711–729. doi: 10.1175/2008JCLI2542.1
- Maloney, E. D. and Chelton, D. (2006). An Assessment of the Sea Surface Temperature Influence on Surface Wind Stress in Numerical Weather Prediction and Climate Models. *J. Clim.* 19, 2743–2762. doi: 10.1175/JCLI3728.1
- Meehl, G. A., Covey, C., Delworth, T. L., Latif, M., McAvaney, B. J., Mitchell, J. F. B., et al. (2007). The Wcrp Cmp3 Multimodel Dataset: A New Era in Climate Change Research. *Bull. Am. Meteorol. Soc.* 88, 1383–1394. doi: 10.1175/BAMS-88-9-1383
- Meng, Z., Zhou, L., Murtugudde, R., Yang, Q., Pujiana, K. and Xi, J. (2021). Tropical Oceanic Intraseasonal Variabilities Associated With Central Indian Ocean Mode. *Clim. Dyn.* 58, 1107–1126. doi: 10.1007/s00382-021-05951-1
- Murtugudde, R. G., Busalacchi, A. J. and Beauchamp, J. (1998). Seasonal-To-Interannual Effects of the Indonesian Throughflow on the Tropical Indo-Pacific Basin. *J. Geophys. Res.* 103, 21425–21441. doi: 10.1029/98JC02063
- Murtugudde, R., McCreary, J. P. and Busalacchi, A. J. (2000). Oceanic Processes Associated With Anomalous Events in the Indian Ocean With Relevance to 1997–1998. *J. Geophys. Res.* 105, 3295–3306. doi: 10.1029/1999JC900294
- Neelin, J. D., Held, I. M. and Cook, K. H. (1987). Evaporation-Wind Feedback and Low-Frequency Variability in the Tropical Atmosphere. *J. Atmos. Sci.* 44, 2341–2348. doi: 10.1175/1520-0469(1987)044<2341:EWFAF>2.0.CO;2
- Pypker, B. J. and Peterman, R. M. (1998). Comparison of Methods to Account for Autocorrelation in Correlation Analyses of Fish Data. *Can. J. Fish. Aquat. Sci.* 55, 2127–2140. doi: 10.1139/f98-104
- Qin, J., Zhou, L., Li, B. and Murtugudde, R. (2020). Simulation of Central Indian Ocean Mode in S2S Models. *J. Geophys. Res.* 125, e2020JD033550. doi: 10.1029/2020JD033550
- Qin, J., Zhou, L., Meng, Z., Li, B., Lian, T. and Murtugudde, R. (2021). Barotropic Energy Conversion During Indian Summer Monsoon: Implication of Central Indian Ocean Mode Simulation in CMIP6. *Clim. Dyn.* 58, 3187–3206. doi: 10.21203/rs.3.rs-715759/v1
- Quadfasel, D. and Cresswell, G. R. (1992). A Note on the Seasonal Variability of the South Java Current. *J. Geophys. Res.* 97, 3685–3688. doi: 10.1029/91JC03056
- Rajendran, K. and Kitoh, A. (2006). Modulation of Tropical Intraseasonal Oscillations by Ocean-Atmosphere Coupling. *J. Clim.* 19, 366–391. doi: 10.1175/JCLI3638.1
- Ratna, S. B., Cherchi, A., Osborn, T. J., Joshi, M. M. and Uppara, U. (2021). The Extreme Positive Indian Ocean Dipole of 2019 and Associated Indian Summer Monsoon Rainfall Response. *Geophys. Res. Lett.* 48, e2020GL091497. doi: 10.1029/2020GL091497
- Rodwell, M. J. W. (1997). Breaks in the Asian Monsoon: The Influence of Southern Hemisphere Weather Systems. *J. Atmos. Sci.* 54, 2597–2611. doi: 10.1175/1520-0469(1997)054<2597:BITAMT>2.0.CO;2
- Roxy, M. K. and Tanimoto, Y. (2007). Role of SST Over the Indian Ocean in Influencing the Intraseasonal Variability of the Indian Summer Monsoon. *J. Meteorol. Soc. Jpn.* 85, 349–358. doi: 10.2151/jmsj.85.349
- Saji, N. H., Goswami, B. N., Vinayachandran, P. N. M. and Yamagata, T. (1999). A Dipole Mode in the Tropical Indian Ocean. *Nature* 401, 360–363. doi: 10.1038/43854
- Saji, N. H. and Yamagata, T. (2003). Possible Impacts of Indian Ocean Dipole Mode Events on Global Climate. *Clim. Res.* 25, 151–169. doi: 10.3354/cr025151
- Shi, P., Lu, H., Leung, L. R., He, Y., Wang, B., Yang, K., et al. (2021). Significant Land Contributions to Interannual Predictability of East Asian Summer Monsoon Rainfall. *Earth. Future* 9, e2020EF001762. doi: 10.1029/2020EF001762
- Small, R. J., Deszoeke, S. P., Xie, S., O'Neill, L. W., Seo, H., Song, Q., et al. (2008). Air-sea Interaction Over Ocean Fronts and Eddies. *Dyn. Atmos. Ocean.* 45, 274–319. doi: 10.1016/j.dynatmoce.2008.01.001
- Sobel, A. H., Maloney, E. D., Bellon, G. and Frierson, D. M. (2008). The Role of Surface Heat Fluxes in Tropical Intraseasonal Oscillations. *Nat. Geosci.* 1, 653–657. doi: 10.1038/ngeo312
- Suhas, E., Neena, J. M. and Goswami, B. N. (2012). An Indian Monsoon Intraseasonal Oscillations (MISO) Index for Real Time Monitoring and Forecast Verification. *Clim. Dyn.* 40, 2605–2616. doi: 10.1007/s00382-012-1462-5
- Taylor, K. E., Stouffer, R. J. and Meehl, G. A. (2012). An Overview of CMIP5 and the Experiment Design. *Bull. Am. Meteorol. Soc.* 93, 485–498. doi: 10.1175/BAMS-D-11-00094.1
- Vialard, J., Foltz, G. R., McPhaden, M. J., Duvel, J. P., and Montégut, C. de B. (2008). Strong Indian Ocean Sea Surface Temperature Signals Associated With the Madden-Julian Oscillation in Late 2007 and Early 2008. *Geophys. Res. Lett.* 35, L19608. doi:10.1029/2008GL035238.
- Vinayachandran, P. N. M. and Saji, N. H. (2008). Mechanisms of South Indian Ocean Intraseasonal Cooling. *Geophys. Res. Lett.* 35, L23607. doi: 10.1029/2008GL035733
- Wang, B., Ding, Q., Fu, X., Kang, I.-S., Jin, K., Shukla, J., et al. (2005). Fundamental Challenge in Simulation and Prediction of Summer Monsoon Rainfall. *Geophys. Res. Lett.* 32, L15711. doi: 10.1029/2005GL022734
- Wang, B., Lee, J.-Y. and Xiang, B. (2014). Asian Summer Monsoon Rainfall Predictability: A Predictable Mode Analysis. *Clim. Dyn.* 44, 61–74. doi: 10.1007/s00382-014-2218-1
- Webster, P. J. (1983). Mechanisms of Monsoon Low-Frequency Variability: Surface Hydrological Effects. *J. Atmos. Sci.* 40, 2110–2124. doi: 10.1175/1520-0469(1983)040<2110:MOMLFV>2.0.CO;2
- Weng, S.-P. and Yu, J.-Y. (2010). A CGCM Study on the Northward Propagation of Tropical Intraseasonal Oscillation Over the Asian Summer Monsoon Regions. *Terr. Atmos. Ocean. Sci.* 21, 299–312. doi: 10.3319/TAO.2009.02.18.01(A)
- Xie, S. (2004). Satellite Observations of Cool Ocean-Atmosphere Interaction. *Bull. Am. Meteorol. Soc.* 85, 195–208. doi: 10.1175/BAMS-85-2-195
- Xie, S. and Philander, S. G. (1994). A Coupled Ocean-Atmosphere Model of Relevance to the ITCZ in the Eastern Pacific. *Tellus*. A. 46, 340–350. doi: 10.3402/tellusa.v46i4.15484
- Xi, J., Zhou, L., Murtugudde, R. and Jiang, L. (2015). Impacts of Intraseasonal SST Anomalies on Precipitation During Indian Summer Monsoon. *J. Clim.* 28, 4561–4575. doi: 10.1175/JCLI-D-14-00096.1
- Yu, L., and Weller, R. A. (2007). Objectively Analyzed Air-Sea Heat Fluxes for the Global Ice-Free Oceans (1981–2005). *Bull. Am. Meteorol. Soc.* 88, 527–540. doi: 10.1175/BAMS-88-4-527
- Zhou, L. and Murtugudde, R. (2014). Impact of Northward-Propagating Intraseasonal Variability on the Onset of Indian Summer Monsoon. *J. Clim.* 27, 126–139. doi: 10.1175/JCLI-D-13-00214.1
- Zhou, L., Murtugudde, R., Chen, D. and Tang, Y. (2017a). A Central Indian Ocean Mode and Heavy Precipitation During the Indian Summer Monsoon. *J. Clim.* 30, 2055–2067. doi: 10.1175/JCLI-D-16-0347.1

- Zhou, L., Murtugudde, R., Chen, D. and Tang, Y. (2017b). Seasonal and Interannual Variabilities of the Central Indian Ocean Mode. *J. Clim.* 30, 6505–6520. doi: 10.1175/JCLI-D-16-0616.1
- Zou, L. and Zhou, T. (2016). A Regional Ocean–Atmosphere Coupled Model Developed for CORDEX East Asia: Assessment of Asian Summer Monsoon Simulation. *Clim. Dyn.* 47, 3627–3640. doi: 10.1007/s00382-016-3032-8

Conflict of Interest: The authors declare that the research was conducted in the absence of any commercial or financial relationships that could be construed as a potential conflict of interest.

Publisher’s Note: All claims expressed in this article are solely those of the authors and do not necessarily represent those of their affiliated organizations, or those of the publisher, the editors and the reviewers. Any product that may be evaluated in this article, or claim that may be made by its manufacturer, is not guaranteed or endorsed by the publisher.

Copyright © 2022 Meng, Zhou, Qin and Li. This is an open-access article distributed under the terms of the Creative Commons Attribution License (CC BY). The use, distribution or reproduction in other forums is permitted, provided the original author(s) and the copyright owner(s) are credited and that the original publication in this journal is cited, in accordance with accepted academic practice. No use, distribution or reproduction is permitted which does not comply with these terms.